

Available online at www.sciencedirect.com

jmr&t
Journal of Materials Research and Technology
journal homepage: www.elsevier.com/locate/jmrt



Original Article

Microstructure and corrosion resistance of novel β -type titanium alloys manufactured by selective laser melting



D. Pede ^{a,b,*}, M. Li ^b, L. Virovac ^b, T. Poleske ^b, F. Balle ^c, C. Müller ^a,
H. Mozaffari-Jovein ^b

^a Department of Microsystems Engineering, IMTEK, University of Freiburg, Georges-Köhler-Allee 103, D-79110 Freiburg, Germany

^b Institute of Materials Science and Engineering Tuttlingen, IWAT, Furtwangen University, Kronenstraße 16, D-78532 Tuttlingen, Germany

^c Department of Sustainable Systems Engineering, INATECH, University of Freiburg, Emmy-Noether-Straße 2, D-79110 Freiburg, Germany

ARTICLE INFO

Article history:

Received 17 March 2022

Accepted 4 July 2022

Available online 8 July 2022

Keywords:

Titanium alloys

Additive manufacturing

Selective laser melting

Microstructure

Corrosion

Corrosion products

ABSTRACT

Due to its unique characteristics selective laser melting offers the possibility to manufacture highly complex and functional parts out of otherwise difficult processable materials. One example is β -type titanium alloys, which have very promising properties for various engineering applications. Two novel β -type alloys Ti–42Nb and Ti–20Nb–6Ta were compared with commercially pure titanium and Ti–6Al–4V ELI alloy in this study. All four lightweight materials were SLM-processed and the microstructure and corrosion resistance were investigated. While pure titanium and Ti–6Al–4V showed only the martensitic α' -phase, Ti–42Nb consists solely of the β -phase and Ti–20Nb–6Ta of the orthorhombic martensitic α'' -phase. Potentiodynamic polarization showed a superior corrosion resistance for both β -type alloys, whereas Ti–42Nb performed slightly better than Ti–20Nb–6Ta. Released V and Al could be clearly observed for the Ti–6Al–4V ELI alloy by mass spectrometry due to corrosion processes, in contrast the release of Nb or Ta was hardly detected for the new alloys.

© 2022 The Author(s). Published by Elsevier B.V. This is an open access article under the CC BY-NC-ND license (<http://creativecommons.org/licenses/by-nc-nd/4.0/>).

1. Introduction

Due to the outstanding combination of low density, high specific strength, good biocompatibility, good corrosion

resistance and high fatigue strength, titanium and its alloys have been widely used in various industrial sectors such as aerospace, biomedical engineering, nuclear, marine and chemical industry [1]. As an allotrope material pure titanium crystallizes in a high-temperature body-centered cubic (bcc) β -

* Corresponding author.

E-mail address: dennis.pede@hs-furtwangen.de (D. Pede).

<https://doi.org/10.1016/j.jmrt.2022.07.021>

2238-7854/© 2022 The Author(s). Published by Elsevier B.V. This is an open access article under the CC BY-NC-ND license (<http://creativecommons.org/licenses/by-nc-nd/4.0/>).

phase and reversibly transforms into a low-temperature hexagonal close-packed (hcp) α -phase at β -transus temperature 882 °C [1,2]. Both phases can be stabilized by the addition of different alloying elements. Depending on the chosen elements and their amount it is possible to control the amount and distribution of the two phases in the resulting microstructure [1,3]. Thereby α -type, β -type or $\alpha+\beta$ -type titanium alloys can be obtained and the material properties can be tailored to specific needs [2,3]. Commercially pure titanium (cp-Ti) is a prominent and widely used example for a titanium-based material consisting only of α -phase. One major drawback is the rather low mechanical properties, which resulted in the development of different kind of $\alpha+\beta$ -type Ti alloys with superior strength, hardness and toughness, such as Ti–6Al–4V or Ti–6Al–7Nb [1–3].

Recently β -type Ti alloys have received an increasing interest due to the unique combination of reasonable strength [4], low elastic modulus [5], excellent corrosion resistance [6] and workability [7]. Corrosion resistance plays an immense role if β -type Ti alloys are going to be used for aerospace, chemical, medical or marine applications. The excellent corrosion resistance of titanium is mainly based on its high affinity towards oxygen, that leads to the spontaneous formation of a protective and self-repairing passive layer on the surface, which mainly composes of TiO₂ [1,8]. As previously investigated by other studies different alloying elements can have an influence on the oxide layer, e.g., its composition, density and stability [6]. Studies have shown that certain β stabilizing elements can promote the spontaneous passivation and lead to the formation of a compact oxide layer [9–11]. Niobium and tantalum are both promising β stabilizing alloying elements as they can suppress the phase transformation from β into α [12] and form a compact oxide layer, resulting in an enhanced corrosion resistance [13–15]. Additionally, they can improve the biocompatibility [16–18] and reduce the elastic modulus [19] of Ti-based alloys. For example, binary Ti–Nb alloys containing Nb in the range of 10–20 wt.% and 35–50 wt.% exhibit an elastic modulus around 60–70 GPa with a minimum of around 62 GPa at 42 wt.% Nb, as reported by Hon et al. [20] and Ozaki et al. [21]. Schulze et al. [22] have shown an elastic modulus of 60 GPa for a Ti–42Nb alloy processed by selective laser melting, that also exhibit an improved cell tolerance in comparison to Ti–6Al–4V [23]. However, studies have shown, that ternary Ti–Nb–Ta alloys can exhibit a comparable low elastic modulus, too [24,25]. Furthermore, the addition of Ta to a binary Ti–Nb alloy can enhance superconductive properties, improve the resistance against corrosion fatigue cracking and suppress the formation of the ω -phase, which can be detrimental to the mechanical properties [26–28].

In the last decade, additive manufacturing (AM) has become an increasingly important process in various industries, since products with customized requirements and complex geometries can be manufactured almost near-net-shape due to the high degree of design freedom [29,30]. Disadvantages of conventional subtractive processes such as high material consumption and multi-stage post-processing can be overcome [31].

Selective laser melting (SLM) is one of the most promising technologies as it can process a wide range of different pure

metals and alloys and produce almost completely dense parts [31,32]. It is a powder bed-based process, where a focused laser beam is used to melt a layer of metallic powder according to a computer-aided design (CAD) model and the part is built layer-wise [32]. Furthermore, it has the advantage of processing powder materials to fabricate complex designs without the need of extensive post-treatment. Nowadays, a wide variety of different metals and alloys can be successfully processed with SLM, like Fe alloys, Al alloys, Ni alloys and even different refractory metals and alloys [32,33]. Therefore, SLM can also help to process alloys containing elements such as Nb and Ta in a more effective way. Usually such alloys are arc melted and subtractive machined [34,35]. This is often highly time and cost consuming as the alloys are not easy to be processed due to their high strength and hardness.

Besides the mentioned materials, titanium is a further prominent example. Due to the wide application in various industrial sectors especially pure titanium and the Ti–6Al–4V alloy have been intensively researched as materials for SLM during the last decade [36–38]. Thijs et al. [39] analyzed the microstructure of Ti–6Al–4V after SLM and found out, that the solidification conditions give rise to a martensitic phase and could lead to the precipitation of an intermetallic phase. Xu et al. [40] investigated the microstructure, mechanical properties and corrosion behavior of SLM-processed Ti–6Al–4V and reported an inferior corrosion resistance compared to conventionally processed Ti–6Al–4V, whereas a post-annealing treatment could reduce the susceptibility to corrosion. The corrosion behavior of SLM produced Ti–6Al–4V in Hank's solution was investigated by Cui et al. [41], which discovered a frequent metastable pitting of the material compared to an annealed counterpart caused by a higher amount of cation vacancies contributing to pit nucleation. Wysocki et al. [42] characterized the microstructure and mechanical properties of pure titanium processed by SLM, whereas a slight amount of oxygen was added during the process. They reported superior mechanical properties compared to conventionally processed titanium as a result of oxygen solution strengthening.

Although the current state of scientific knowledge is still not comparable to the extensive research done on α - and $\alpha+\beta$ -type Ti alloys, several studies have been done on β -type titanium alloys and SLM in the recent years as well. Various groups have investigated different combinations of Ti with elements like Fe, Nb, Mo, Si, Sn, V, Ta or Zr [33]. Wang et al. [43] have manufactured a Ti–35Nb composite from elemental powder mixture using SLM and investigated the microstructure, mechanical behavior and corrosion resistance. A Ti–6Al–4V–10Mo alloy was also manufactured from elemental powder mixture and analyzed regarding its microstructure and mechanical properties by Vrancken et al. [44]. Hariharan et al. [45] studied the mechanical and corrosion properties of an SLM-processed and heat treated near β -type Ti–13Nb–13Zr alloy. Zhou et al. [46] added different amounts of Ta to a Ti–13Nb–13Zr alloy and analyzed the phase transformations during SLM. The influence of different Si contents on the properties of a SLM processed Ti–Nb–Zr–Ta alloy was investigated by Luo et al. [47].

In this study four different titanium-based materials, cp-Ti (α -type), Ti–6Al–4V ($\alpha+\beta$ -type) and the two β -type Ti alloys Ti–42Nb and Ti–20Nb–6Ta were additively manufactured

using SLM. The microstructure was characterized with X-ray diffraction and metallography. To investigate the corrosion resistance of the materials potentiodynamic polarization was used and the electrolyte was subsequently analyzed with mass spectrometry, to qualitatively and quantitatively determine alloying elements that were released due to anodic metal dissolution. Furthermore, the surface of several specimens was machined prior to the electrochemical experiments and the performance compared to the SLM as-built surface. Surface characterizations, such as profilometry and optical microscopy, were used to examine the surface morphology.

2. Experimental details

2.1. Materials and sample preparation

Four different titanium-based powder materials in the form of cp-Ti grade 2 (Concept Laser), Ti–6Al–4V ELI (Concept Laser), Ti–42Nb (Taniobis) and Ti–20Nb–6Ta (Taniobis) were used. The chemical compositions of the powder materials are shown in Table 1.

With a SLM apparatus (Concept Laser, Mlab cusing 100 R) specimens in the shape of cylindrical rods with a diameter of 9.5 mm and height of 12.7 mm were fabricated under argon atmosphere. The used process parameters and resulting relative densities (determined by Archimedes method) can be seen in Table 2.

The specimens were divided into three groups for subsequent treatment processes and investigation. One group of specimens was used in its originally as-built state and wasn't subjected to any post treatments, while two groups had their surface machined to eliminate the influence of the surface condition on the corrosion resistance. One group was machined by a simple turning process with a TiN coated cutting tool, cutting speed of 33 mm/min and feed rate of 0.1 mm/r. The second group was semi manually grounded up to 2500 grit with silicon carbide (SiC) paper and polished up to 6000 grit with silicon cloth (3 M™ Hookit™ Trizact™ 6000). The resulting surface morphology was investigated with optical microscopy (OM, Keyence, VHX-5000) exemplarily for one specimen before and after conducting the electrochemical experiments. Furthermore, the surface roughness of every specimen was determined as the arithmetic mean surface deviation R_a with a surface profilometer (Zeiss, TSK Roughness Tester).

2.2. Microstructure observation and phase analysis

Phase identifications were conducted on polished specimens by a X-ray diffractometer (XRD, Bruker, D8 Discovery) using

Table 1 – Chemical compositions of the powder materials (in wt.%).

Material	Ti	Al	V	Nb	Ta	Fe
Cp-Ti	Bal.	–	–	–	–	0.11
Ti–6Al–4V	Bal.	7.26	4.24	–	–	0.09
Ti–42Nb	Bal.	–	–	41.7	–	0.06
Ti–20Nb–6Ta	Bal.	–	–	21.31	5.41	0.04

Table 2 – Used SLM process parameters with the relative density for each material.

	P (W)	v_s (mm/s)	h_s as d_L (μm)	d_L (μm)	Rel. density (%)
Cp-Ti	68.00	525.00	100.00	25.00	99.98
Ti–6Al–4V	95.00	900.00	100.00	25.00	99.99
Ti42Nb	95.00	400.00	100.00	25.00	99.99
Ti–20Nb–6Ta	95.00	900.00	75.00	25.00	99.99

monochromatic Cu $K\alpha$ radiation and a voltage of 40 kV with a scanning rate of 0.04°/s in the range of 2θ from 30° to 80°. Further microstructure observation was done with a Zeiss EVO MA 15 scanning electron microscope (SEM) on metallographic specimens that were cut out of SLM manufactured parts, prepared by standard metallographic techniques and subsequently etched with Kroll's reagent (10 vol% HF and 5 vol% HNO₃).

2.3. Electrochemical investigations

Before the electrochemical tests, all specimens were cleaned in an ultrasonic bath in ethanol for 15 min, rinsed with ethanol and dried. To assure a comparable surface a waterproof adhesive (Henkel, M–121HP HYSOL) was used to cover the frontal and basal surfaces of all specimens, so that only the lateral surface was exposed during the tests.

The pitting corrosion resistance was studied by potentiodynamic polarization, which was performed in a temperature controlled electrochemical cell using a three-electrode assembly connected by a Gamry Interface 1000 potentiostat. The specimens served as the working electrode, a graphite rod and silver chloride electrode (Ag/AgCl/3 M KCl) were used as counter electrode and reference electrode, respectively. Ultrapure deionized water (resistivity $\geq 18.2 \text{ M}\Omega \text{ cm}$ at 25 °C) was used to prepare a 0.9 wt.% NaCl solution as the electrolyte, which was kept at a constant temperature of $37 \pm 1 \text{ }^\circ\text{C}$ (Lauda, ECO Silver) during the experiments to imitate human body conditions. At the start of each measurement, the open circuit potential (OCP) was recorded over a period of 2 h, allowing stabilization. The following potentiodynamic polarization experiments were done with a sweep range from -0.5 V to 10 V versus OCP voltage at a constant sweep rate of 1 mV/s. All potentials included in this study are referred to the standard hydrogen electrode (SHE). The polarization experiments were repeated at least three times with different specimens. The corrosion potential (E_{corr}) and corrosion current density (i_{corr}) were calculated via tafel extrapolation method. The polarization resistance (R_p) was calculated by using the Stern–Geary equation [48],

$$R_p = \frac{\beta_a \cdot \beta_c}{2.3 \cdot i_{\text{corr}} (\beta_a \cdot \beta_c)} \quad (1)$$

where β_a and β_c are the anodic and cathodic slopes of the corresponding Tafel plot. Other values were extracted from the polarization curves.

2.4. Mass spectrometric analysis

After potentiodynamic polarization the electrolytes were further investigated with inductively coupled plasma mass spectrometry (ICP-MS). A Thermo Scientific™ iCAP™ RQ

ICP–MS in standard mode (without a collision gas) and in kinetic energy discrimination (KED) mode (with He as a collision gas) with the SC-4 DX Autosampler (Elemental Scientific) were used. Preparation of necessary calibration solutions was done with 10 $\mu\text{g}/\text{mL}$ Al, V, Nb and Ta single element standard solutions (Inorganic Ventures). Ge single element standard (Inorganic Ventures) was used as intern standard. Samples and standard solutions were prepared and diluted with high purity nitric acid 67–69% (VWR Chemicals) and ultrapure deionized water. 2 wt.% nitric acid was used as blank.

3. Results

3.1. Microstructure characterization

Selected XRD spectra of cp-Ti, Ti–6Al–4V, Ti–42Nb and Ti–20Nb–6Ta are depicted in Fig. 1. The XRD results suggest that cp-Ti and Ti–6Al–4V only consists of hexagonal α (hcp) or martensitic α' . As both phases have the same hcp crystal structure and overlap in the diffractogram, they could not be clearly distinguished. Furthermore, no clear peak of the bcc β -phase could be detected for Ti–6Al–4V, despite of the present β stabilizing element V. In contrast for Ti–42Nb, the content of the β stabilizing element Nb was high enough to completely stabilize the β -phase. As a result, the XRD spectrum shows only peaks that corresponds to the bcc crystal structure. However, the other β -type alloy Ti–20Nb–6Ta does neither reveal the existence of α - or α' - nor β -phase in the diffraction spectrum, but solely consists of martensitic orthorhombic α'' -phase.

For further microstructural characterization and clarification of the XRD results SEM images of the microstructure of all four titanium-based materials are illustrated in Fig. 2. Cp-Ti and Ti–6Al–4V show a microstructure composed of large amounts of acicular structures with a length of a few to several tens of micrometers and a width of up to hundreds of nanometers (Fig. 2a, b). Additionally, the structure of Ti–6Al–4V showed a kind of texture as lots of needles are

aligned perpendicular which leads to a meshed pattern of α' needles. No sign of β -phase can be detected in the images as predicted by the diffractogram.

In contrast to Ti–42Nb and Ti–20Nb–6Ta (Fig. 2c, d), the microstructures exhibit a different form. What can be seen are clearly visible grain boundaries and the retained contours of the melt pools that were created during the SLM process (indicated by white arrows). Furthermore, when observed at a higher magnification, a cellular substructure is visible for both alloys. Ti–20Nb–6Ta additionally shows some acicular structures with the length of a few to tens of micrometers and width of hundreds of nanometers, indicated by black arrows.

3.2. Surface condition

Figure 3 shows the OM images of the unmachined and machined surfaces for the studied materials. Images of the as-built condition (Fig. 3a, d, g and j) show the typical surface of SLM-manufactured specimens, where partially melted particles cover the surface (black arrows) and lead to a high roughness. The turning process (Fig. 3b, e, h and k) successfully removed the residual powder particles from the surface, but additionally led to typical turning grooves and marks (black arrows) as result of a localized excessive material removal. After grinding and polishing (Fig. 3c, f, i and l) the residual powder particles were removed successfully as well, but the surfaces also exhibit a rather smooth condition with only minor grooves and slight scratches (black arrows). A pronounced difference between the studied materials cannot be observed.

Table 3 lists the determined arithmetic mean surface deviation R_a for different samples with different surface treatment methods every material.

The SLM process without post treatments, led to the roughest surface with Ti–20Nb–Ta, which showed a 2.8–3.5 times higher value than the other materials. While cp-Ti, Ti–6Al–4V and Ti–42Nb demonstrated similar values. The turning of the surfaces drastically reduced the roughness. The precise surface treatment via grinding and polishing resulted in comparable and very smooth surfaces with a R_a of 0.05 μm –0.08 μm .

3.3. Open circuit potential

The variations of OCP for cp-Ti, Ti–6Al–4V, Ti–42Nb and Ti–20Nb–6Ta with their unmachined as-built surface are presented in Fig. 4. It can be seen that Ti–6Al–4V has a very steady potential and almost instantly reaches a stable value of 0.026 mV. However, it is the only material with a positive OCP. Cp-Ti shows some fluctuations at the start of the measurement, until the potential begins to level out after 1500 s and approaches a value of -0.272 V. The Ti–20Nb–6Ta specimen seems to approach a certain potential right from the start, but instead of reaching a stable value the OCP is constantly fluctuation around a potential of around -0.475 V and does not level out. The OCP of Ti–42Nb is the only one that starts at a lower potential and shows a pronounced shift to a more noble potential. The value steadily increases, until it apparently keeps stable at a potential of -0.432 V.

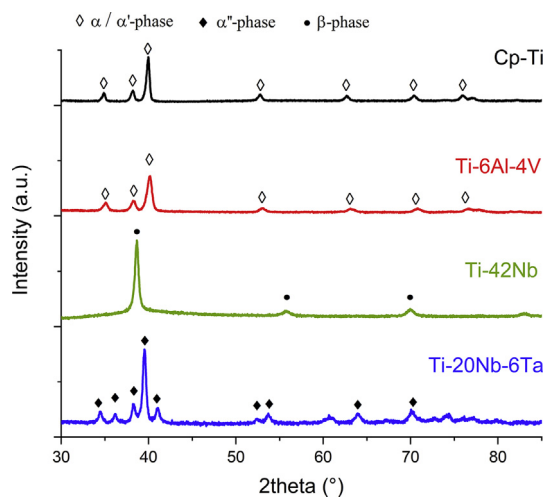


Fig. 1 – XRD spectra for SLM-processed cp-Ti, Ti–6Al–4V, Ti–42Nb and Ti–20Nb–6Ta.

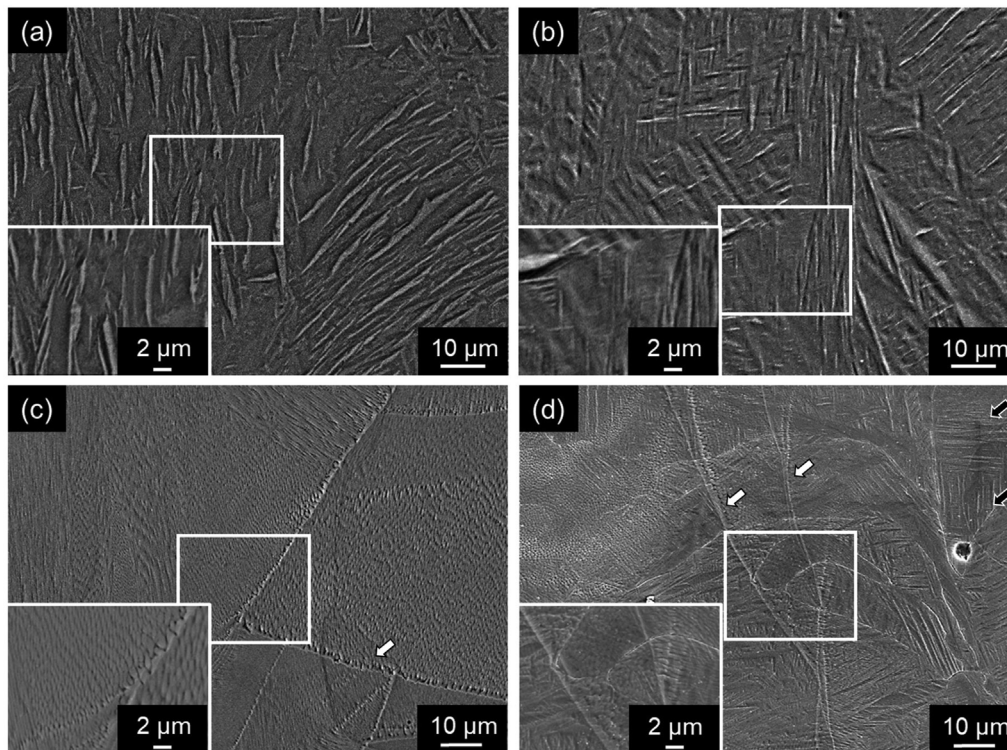


Fig. 2 – SEM micrographs of (a) cp-Ti, (b) Ti–6Al–4V, (c) Ti–42Nb and (d) Ti–20Nb–6Ta. The white arrows indicate the melt pool boundaries, the black arrows indicate acicular structures in the Ti–20Nb–6Ta alloy.

Figure 5 display the OCP curves for each material after the surface machining by a turning process. Except for cp-Ti the potentials of the studied materials are steadily increasing over time and approaching a stable value, which is, however, not reached after 2 h. Ti–6Al–4V shows the highest potential of -0.142 V at the end of the measurement, whereas Ti–20Nb–6Ta has the lowest OCP of -0.427 V. Cp-Ti again exhibits pronounced fluctuations at the initial stage, this time up to 3500 s, and then keeps stable at a value about -0.224 V.

The variation of OCP with immersion time for SLM-processed cp-Ti, Ti–6Al–4V, Ti–42Nb and Ti–20Nb–6Ta with a grinded and polished surface was elaborated as well (Fig. 6). Cp-Ti and Ti–6Al–4V show a similar behavior as they do not show any major fluctuations and reach an almost stable value of -0.343 V and -0.432 V, respectively, right from the beginning of the OCP measurement. The OCP curve of Ti–20Nb–6Ta shows an initial peak and increase, which is flattening after 3000 s of immersion time and then keeping a stable value around -0.407 V. Ti–42Nb displays an initial, but less pronounced peak as well. Subsequently, the potential slightly, but steadily decreases and reaches a value of -0.238 V after 7200 s and the most positive OCP of the studied materials.

3.4. Potentiodynamic polarization

The polarization curves of cp-Ti, Ti–6Al–4V, Ti–42Nb and Ti–20Nb–6Ta with different surface post treatment processes are depicted in Figs. 7–9 with the determined corrosion parameters listed in Table 4. In general, it is visible that all four

materials exhibit a typical cathodic (until E_{corr}) and anodic-passive region, while an anodic-transpassive (starting at E_{break}) region is only present for cp-Ti and Ti–6Al–4V. The passive region is normally initiated at a potential E_{crit} and characterized by i_{pass} , but the investigated materials exhibit a second passive region (defined by $i_{\text{pass}2}$), that takes place after a local maximum i_{peak} at the potential E_{peak} was reached.

Figure 7 shows the results of the potentiodynamic polarization with the SLM as-built surface. The transition from the cathodic in the anodic region at E_{corr} is visible for all materials with Ti–6Al–4V having the highest value. The respective corrosion current density i_{corr} is the highest for Ti–20Nb–6Ta and the lowest for Ti–42Nb. Subsequently, the current density is increasing for all materials as anodic dissolution and passive layer formation takes place until a passive region is reached, initiated at E_{peak} . Since no clear passive region is visible, no critical potential E_{crit} or passivation current density i_{pass} could be determined. As the current density increases it reaches a maximum i_{peak} at E_{peak} , where cp-Ti displays the lowest current density. With further increase of the potential after E_{peak} the β -type alloys show a stable passive behavior with no transpassive region until the maximum potential of 10 V, whereas Ti–6Al–4V and cp-Ti show a breakdown of their passive layer and transition into the transpassive region at the respective potential E_{break} .

In Fig. 8 the polarization curves for the materials with turned surfaces are shown. Similar to the specimens with the SLM as-built surface Ti–20Nb–6Ta has the lowest E_{corr} , while Ti–Al–4V has the highest. In contrast to the SLM as-built surface all specimens with the turned surface show a

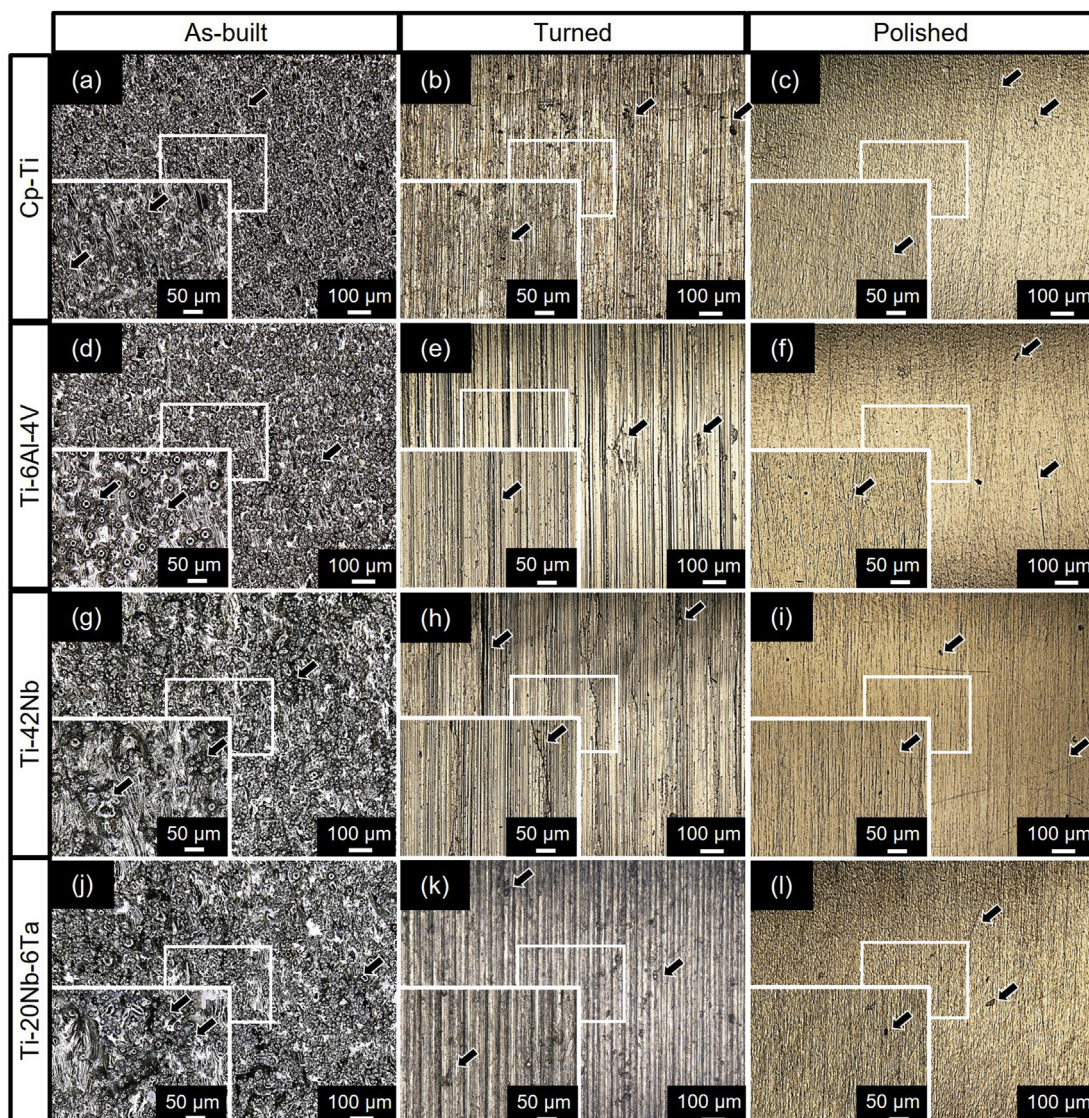


Fig. 3 – OM images of SLM-processed cp-Ti, Ti-6Al-4V, Ti-42Nb and Ti-20Nb-6Ta specimens with unmachined (as-built, left) and machined surfaces (turned middle, polished right) before polarization experiments.

pronounced first passive region marked by E_{crit} and characterized by i_{pass} . Ti-20Nb-6Ta is the first material to reach the passive region, whereas Ti-6Al-4V is the last one but displays the lowest passivation current density. The current densities remain stable until they increase again and reach a local maximum at E_{peak} . Whereas E_{peak} is rather similar for the four materials at a range of 1.831–1.841 V, i_{peak} differs between the

materials. Cp-Ti exhibits the highest, Ti-42Nb and Ti-20Nb-6Ta have the same and Ti-6Al-4V shows the lowest current density. As the polarization goes on, Ti-6Al-4V quickly reaches E_{break} first and cp-Ti secondly. Both Ti-42Nb and Ti-20Nb-6Ta show a second passive region after E_{peak} without a subsequent transpassive region until a potential of 10 V.

The polarization curves with a grinded and polished surface can be seen in Fig. 9. Ti-6Al-4V has the lowest E_{corr} and again the highest i_{corr} . The first material to reach the passive region at E_{crit} is Ti-20Nb-6Ta. Again, with proceeding polarization the current densities start to increase at some point until they reach their maximum i_{peak} at the potential E_{peak} , while the two β -type alloys have a lower E_{peak} than the two other materials. Subsequently, a second passive region is observable for all four materials, although it shows some distinctions depending on the material. cp-Ti and Ti-6Al-4V only show small passive regions, after which the current

Table 3 – Surface condition and roughness for the different materials.

Material	R_a (μm)		
	As-built	Turned	Polished
Cp-Ti	6.07 ± 0.56	0.72 ± 0.08	0.05 ± 0.01
Ti-6Al-4V	8.02 ± 0.28	0.42 ± 0.01	0.06 ± 0.02
Ti-42Nb	7.29 ± 2.11	0.93 ± 0.11	0.06 ± 0.01
Ti-20Nb-6Ta	22.34 ± 3.07	1.17 ± 0.03	0.08 ± 0.01

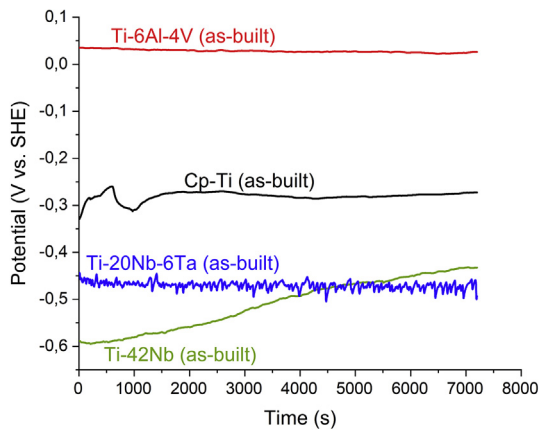


Fig. 4 – OCP of SLM-processed cp-Ti, Ti-6Al-4V, Ti-42Nb and Ti-20Nb-6Ta specimens with unmachined surfaces (as-built condition).

density of both materials starts increasing slightly, but steadily until the transpassive region is reached. The second passive region is more pronounced for Ti-42Nb and Ti-20Nb-6Ta, although a slight increase of the current density of Ti-20Nb-6Ta can be observed at higher potential. Nonetheless, both alloys show no transpassive region until a polarization potential of 10 V.

Table 5 displays the determined anodic and cathodic slopes of the corresponding Tafel plots with the calculated polarization resistance R_p for each material and different surface condition. It can be seen that the value of R_p tends to increase with a machined surface and decreasing surface roughness. Furthermore, with the as-built surface condition Ti-42Nb shows the highest polarization resistance and it descends according to the order Ti-6Al-4V, cp-Ti, Ti-20Nb-6Ta. If the surface was machined, cp-Ti exhibits the highest polarization resistance and the descending order changes to Ti-42Nb, Ti-20Nb-6Ta, Ti-6Al-4V.

After conducting polarization experiments the studied materials were again examined by OM (Fig. 10). The specimens with the as-built surface (Fig. 10a, d, g and j) show signs of

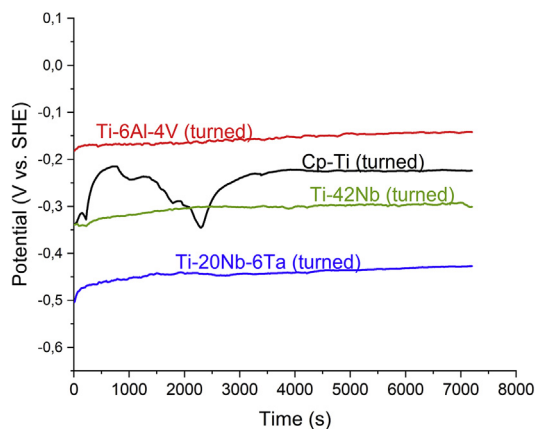


Fig. 5 – OCP of SLM-processed cp-Ti, Ti-6Al-4V, Ti-42Nb and Ti-20Nb-6Ta specimens with turned surfaces.

material removal due to anodic metal dissolution that took place during the experiments, visible in form of less residual powder particles as well as changes of the substrate material (black arrows). It is noteworthy, that these surface morphology changes are much more pronounced for cp-Ti and Ti-6Al-4V than for Ti-42Nb or Ti-20Nb-6Ta, when the images before (Fig. 3a, d, g and j) and after the polarization experiments are compared. If the surfaces were machined by a turning process (Fig. 10b, e, h and k), the corrosion and anodic metal dissolution (black arrows) preferably took place within the turning grooves (white arrows). Cp-Ti and Ti-6Al-4V are covered with several corrosion pits and marks, that are aligned parallel, but more pronounced for Ti-6Al-4V. Furthermore, cp-Ti has some kind of deposition on its surface (white circle). For Ti-42Nb and Ti-20Nb-6Ta no distinct corrosion attack or change of the surface morphology can be noticed, as the recognizable marks (white arrows) were already existent before polarization experiments as a result of the turning process (Fig. 3h and k). After the surfaces were grinded and polished and subjected to potentiodynamic polarization, the surface of cp-Ti is completely covered with several small corrosion pits and marks (black arrows) and shows a blue staining. Ti-6Al-4V shows corrosion pits and marks as well (black arrows), but in comparison to cp-Ti they are bigger. Again, both Ti-42Nb and Ti-20Nb-6Ta show no distinct corrosion attack and the recognizable marks (white arrows) were already existent before polarization experiments (Fig. 3i and l).

3.5. Mass spectrometric analysis

Subsequently to the potentiodynamic polarization experiments the electrolytes were analyzed with mass spectrometry regarding existing alloying elements, that were released due to metallic dissolution. Table 6 lists the results for each material and different surface treatments. Cp-Ti is excluded as it doesn't contain any typical alloying elements. It can be seen that Ti-6Al-4V released its alloying elements V and Al independent of its surface condition. With the surface in its as-built condition the highest amount of Al and V is released, while the amount of Al is more than 2.5 times higher than the amount of V. If a machining process was applied alloying elements were still released, but the actual amount is remarkably reduced. In contrast, Ti-42Nb and Ti-20Nb-6Ta display a completely different behavior. Whereas some Nb is present in the electrolyte for Ti-42Nb with the as-built surface, no remarkable amount of alloying elements can be found after the surface was machined. The same applies for Ti-20Nb-6Ta. Even with the as-built surface, barely any Ta was released. The table lists the value $0.001 \pm 0.001 \mu\text{g/l}$ to indicate the possibility of released Nb and Ta with amounts below the detection limit of the used method.

4. Discussion

4.1. Microstructure evolution

The microstructure of the four different Ti-based materials was investigated. As stated before, Ti-based alloys can be

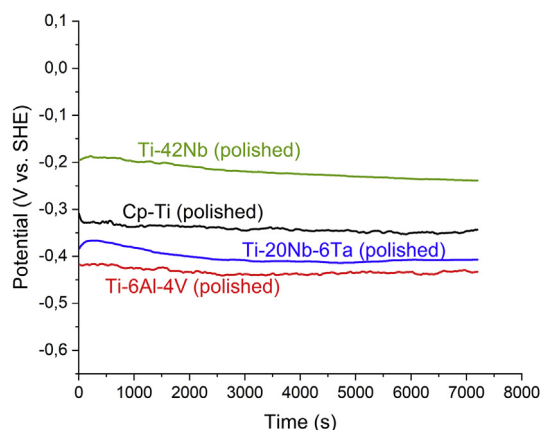


Fig. 6 – OCP of SLM-processed cp-Ti, Ti-6Al-4V, Ti-42Nb and Ti-20Nb-6Ta specimens with grinded and polished surfaces.

classified into three major groups, namely α -phase, heterogeneous $\alpha+\beta$ -phase, and β -phase alloys [1].

However, in addition to the two stable α - and β -phases, several metastable phases such as hcp-martensitic α' , orthorhombic martensitic α'' , and hexagonal or trigonal ω can be formed depending on the alloy composition, cooling rates during quenching, and different thermomechanical treatments [1,3]. The SLM technology is a process, that uses a high-power laser source to melt and subsequently consolidate the metallic powder material [31]. Naturally, due to the high energy input only a very short interaction between the laser beam and the powder particles is necessary to achieve an aggregation change of the metallic material. This, however, results in extremely high cooling rates of at least 10^3 °C/s and rapid solidification processes, which restrain normally occurring diffusion processes and favor the formation of non-equilibrium and metastable phases [39,49–51].

The consequences of these solidification phenomena can be observed in all Ti-based alloys, although the exact expression varies somewhat. In the case of slow solidification, the melt of pure titanium (cp-Ti) crystallizes in the β -phase,

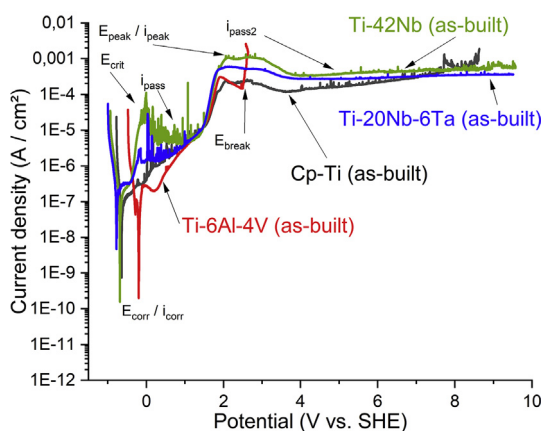


Fig. 7 – Potentiodynamic polarization of SLM-processed cp-Ti, Ti-6Al-4V, Ti-42Nb and Ti-20Nb-6Ta specimens with unmachined surfaces (as-built condition).

which transforms into the α -phase upon further cooling. If the solidification process takes place at faster cooling, α -phase transformation from β into martensitic α' is to be expected. When the Ti-6Al-4V alloy is quenched from the β -phase region at moderate cooling rates to room temperature, a diffusion-controlled phase transition from β to α takes place. In this process, a nucleus of α -phase forms at the grain boundary of the β -phase and nucleus grows into the β -grain as the temperature continues to drop. The affinity and solubility for V is much higher in β -phase than α -phase, so diffusion processes take place and the β -phase is enriched with V [52]. However, the rapid solidification and limited diffusion rates suppress these mechanisms and prevent the transformation of β into α . The XRD spectra show that both cp-Ti and Ti-6Al-4V have a hexagonal crystal structure (Fig. 1). Both, α and martensitic α' , have a hexagonal crystal structure with very similar lattice parameters, so it is not possible to distinguish between them and verify the present phase based solely on XRD studies. However, SEM micrographs (Fig. 2a, b) have shown the formation of extremely fine acicular structures, which, in combination with the described solidification phenomena and very high cooling rate of the SLM process, can be associated with the martensitic phase. Hence, the results indicate that the present hcp phase can be considered as martensitic α' , and not α . This correlates well with the studies of other groups, where the presence of α' was clearly verified for SLM-processed cp-Ti and Ti-6Al-4V using transmission electron microscopy (TEM) [42,53,54]. Besides the martensitic α' -phase, at least some residual vanadium rich β -phase is expected to be found in the microstructure of Ti-6Al-4V. Both SEM studies (Fig. 2b) and XRD analyses (Fig. 1) provided no evidence for the existence of the β -phase. A suggestion by Xu et al. [40] is that the remaining β -phases may exist as nano-scale domains or extremely fine films surrounding the martensite needles, which are below the detection and resolution limits of XRD and SEM. A prove of this assumption was made by Zhou et al. [53], where more detailed investigations using TEM and selected area electron diffraction (SAED) have shown the existence of bcc β -phase besides hcp α' -phase.

In case of β -type Ti-alloys, the crystallization process of the melt strongly depends on the type and concentration of the β -stabilizing elements involved. These, together with the cooling rate applied, determine the solidification microstructures formed and the possible influences of constitutional supercooling on the solidification process. In binary alloy systems, there is a critical threshold for the concentration of the respective β -stabilizing elements at which 100 vol% of the β -phase is retained after quenching [55]. If concentrations below this value are utilized non-equilibrium and metastable phases will form. Considering binary Ti-alloys with Nb or Ta, a content of 35.0 wt.% of Nb or 45.0 wt.% of Ta is needed to suppress the formation of other phases and obtain a microstructure consisting completely of β -phase [55]. The crystal structure of Ti-Nb alloys is highly sensitive to the Nb content and solidification conditions, besides two stable solid phases (α and β phase) several metastable phases (α' , α'' and ω phase) may appear [56]. Lee et al. [57] have shown, that alloys containing 15 wt.% Nb or less are composed of martensitic α' , whereas compositions of 17.5–25 wt.% give rise to martensitic α'' . With an amount of 27.5 wt.% Nb the bcc β -phase starts to be

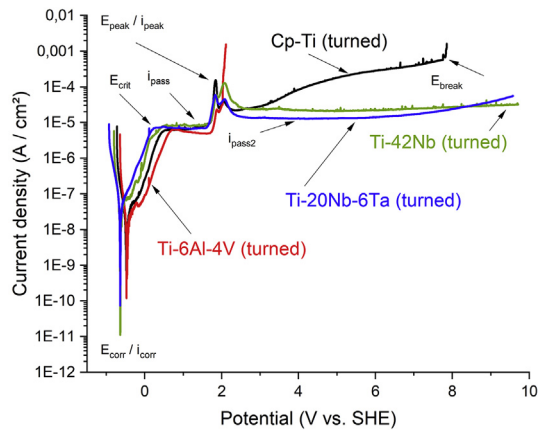


Fig. 8 – Potentiodynamic polarization of SLM-processed cp-Ti, Ti-6Al-4V, Ti-42Nb and Ti-20Nb-6Ta specimens with turned surfaces.

retained and is fully retained at Nb contents of 35 wt.% and higher. The presence of ω -phase could only be detected in alloys with 27.5 and 30 wt.% Nb. Regarding the novel binary Ti-42Nb alloy, the amount of Nb is above the critical concentration of 35 wt.% and therefore the formation of martensite or other metastable phases during quenching is expected to be suppressed. In this work, the XRD spectrum only shows the presence of the β -phase (Fig. 1). Although metastable phases have been found for other SLM processed β -type alloys [33,58], none could be detected herein. The findings corresponds well with the results of other studies with similar alloy compositions [22,59,60]. In contrast to the binary Ti-Nb alloy, the other β -type alloy Ti-20Nb-6Ta does not contain elements above the critical concentrations, so the formation of metastable phases can be expected during quenching. As described before, the findings of Lee et al. [57] suggests a predominant martensitic α'' -phase for a binary Ti-Nb alloy with a similar composition of 17.5–25 wt.%. As shown in (Fig. 1) only peaks of the martensitic orthorhombic α'' are visible, which could be observed in other studies with comparable Ti alloys as well [12,61].

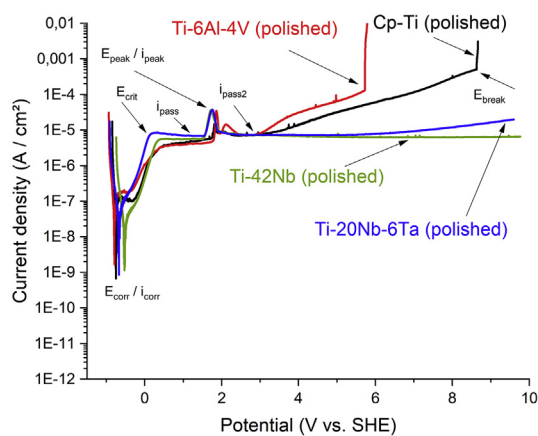


Fig. 9 – Potentiodynamic polarization of SLM-processed cp-Ti, Ti-6Al-4V, Ti-42Nb and Ti-20Nb-6Ta specimens with grinded and polished surfaces.

In the case of Ti-20Nb-6Ta, it is a ternary alloy and an interaction between the alloying elements should be expected. The critical concentrations should be carefully applied. Another useful parameter for describing and comparing the stability of Ti alloys with two or more components is the molybdenum equivalency (MoE). It is a value that considers the combined influence of all alloying elements on the β -phase stability with Mo as an arbitrarily chosen baseline [2,44]. An increasing MoE value usually leads to a decreasing transition temperature of β -phase (T_β), meaning a high MoE value corresponds with a high stability of the β -phase. Furthermore, depending on the MoE value β -type alloys can be sub-divided into near ($5.0 \leq \text{MoE} \leq 10.0$), metastable ($10.0 \leq \text{MoE} \leq 30.0$) and stable ($\text{MoE} > 30.0$) β -type alloys [55]. Near β -type Ti alloys don't have enough β -stabilizing elements to reach the critical concentration, therefore the β -phase is not retained completely during quenching and other phases will form [62]. In metastable alloys the content is high enough to stabilize 100 vol% of the β during quenching [63]. Nonetheless, with subsequent thermo-mechanical treatments phase transformations and tailored microstructures are possible [55]. In the contrary, the so called stable β -type Ti alloys do not undergo phase decomposition [55]. Table 7 summarizes the calculated MoE for the different Ti alloys used in this study. As expected, cp-Ti and Ti-6Al-4V have a rather low MoE value, in terms of Ti-6Al-4V it is even negative. The content of Nb in the Ti-42Nb alloy is very high. Consequently, it also has a high MoE and can be classified as a metastable β -type Ti alloy and is expected to crystallize in the β -phase. The MoE value of the Ti-20Nb-6Ta lies in the range of $5.0 \leq \text{MoE} \leq 10.0$, so this alloy falls into the sub-category of near β -type Ti alloys and metastable phases like α' , α'' or ω can emerge during quenching. These assessments correlate well with the before described results and discussion.

4.2. Corrosion resistance and release of alloying elements

The corrosion resistance of four different Ti-based and SLM processed materials, cp-Ti, Ti-6Al-4V, Ti-42Nb and Ti-20Nb-6Ta, was investigated in terms of the pitting corrosion susceptibility and metallic ion release in a 0.9 wt.% NaCl solution by potentiodynamic polarization. Additionally, two sets of specimens were subjected to turning or grinding and polishing to eliminate the influence of the surface condition, respectively roughness, on the corrosion resistance [64–66].

When processing metals and alloys with additive manufacturing technologies like SLM, different types of volume defects and pores can occur depending on the process parameters and conditions. The different types and causes are discussed elsewhere [67]. Several studies have shown that the presence of porosity can influence and deteriorate the corrosion resistance of additively as well as conventionally manufactured parts. Cao et al. [68] studied the influence of casting porosity on Mg0.1Si and found out, that higher porosity led to a significant higher corrosion rate. Seah et al. [69] investigated porous titanium parts with different level of porosity and pore morphology. They reported that in contrast to large, open, and interconnected pores small, isolated pores deteriorated the corrosion resistance. While open pores enable the free flow of

Table 4 – Surface condition and experimental corrosion parameters for the different materials.

Material	E_{corr} (V)*	i_{corr} (A/cm ²)	E_{crit} (V)*	i_{pass} (A/cm ²)	E_{peak} (V)*	i_{peak} (A/cm ²)	i_{pass2} (A/cm ²)	E_{break} (V)*
Cp-Ti								
As-built	-0.646	0.964×10^{-7}	–	–	2.074	2.398×10^{-4}	–	8.575
Turned	-0.473	0.142×10^{-7}	0.452	6.447×10^{-6}	1.841	1.530×10^{-4}	–	7.754
Polished	-0.749	0.113×10^{-7}	0.394	4.578×10^{-6}	1.812	0.146×10^{-4}	0.069×10^{-4}	8.629
Ti-6Al-4V								
As-built	-0.201	0.621×10^{-7}	–	–	1.907	3.063×10^{-4}	–	2.494
Turned	-0.464	0.832×10^{-7}	0.681	5.187×10^{-6}	1.871	0.231×10^{-4}	–	2.025
Polished	-0.791	0.621×10^{-7}	0.508	4.119×10^{-6}	1.863	0.342×10^{-4}	0.072×10^{-4}	5.726
Ti-42Nb								
As-built	-0.686	0.525×10^{-7}	–	–	2.106	10.800×10^{-4}	4.524×10^{-4}	–
Turned	-0.634	0.213×10^{-7}	0.485	8.193×10^{-6}	1.857	0.598×10^{-4}	0.237×10^{-4}	–
Polished	-0.528	0.152×10^{-7}	0.310	5.542×10^{-6}	1.721	0.364×10^{-4}	0.063×10^{-4}	–
Ti-20Nb-6Ta								
As-built	-0.772	1.870×10^{-7}	–	–	2.140	6.029×10^{-4}	3.207×10^{-4}	–
Turned	-0.636	0.459×10^{-7}	0.200	6.383×10^{-6}	1.831	0.598×10^{-4}	0.128×10^{-4}	–
Polished	-0.681	0.398×10^{-7}	0.144	7.145×10^{-6}	1.755	0.372×10^{-4}	0.072×10^{-4}	–

*The potentials are referred to the standard hydrogen electrode (SHE).

electrolyte and species, closed and small pores promote the trapping of such species and exhaust the supply of oxygen, resulting in weakening of the passive layer and higher corrosion susceptibility. Yang et al. [70] and Sander et al. [71] discovered, that SLM-processed 316L specimens with higher porosity were more prone to metastable and stable pitting, formed unstable passive films that were more susceptible to break-down and repassivation was less expected to happen. The underlying mechanisms for the influence of porosity on the corrosion resistance may be a significantly larger surface area and the restricted transfer of corrosion products and species out of the pores, inducing an auto-catalytic process and favoring the break-down of the protective passive layer [72,73]. However, the used specimens in this study had a high relative density of 99.9%, hence the possible influence of residual pores and defects can be neglected within the frame of this study. Nonetheless, the as-built specimens exhibit a very high roughness and aspects of a porous-like structure, which needs to be considered in this context and will be discussed later.

Table 5 – Surface condition and calculated polarization resistance R_p for the different materials.

Material	β_a (V/dec)	β_c (V/dec)	R_p (Ω cm ²)
Cp-Ti			
As-built	0.942	0.091	3.704×10^5
Turned	0.376	0.204	2.560×10^6
Polished	0.512	0.129	3.986×10^6
Ti-6Al-4V			
As-built	0.697	0.106	6.455×10^5
Turned	0.403	0.094	3.978×10^5
Polished	0.690	0.137	8.002×10^5
Ti-42Nb			
As-built	0.262	0.147	7.802×10^5
Turned	0.395	0.094	1.500×10^6
Polished	0.350	0.107	2.346×10^6
Ti-20Nb-6Ta			
As-built	0.921	0.122	2.502×10^5
Turned	0.400	0.157	1.071×10^6
Polished	0.397	0.121	1.016×10^6

The OCP plots of each material with the different surface conditions were described before (Figs. 4–6). What can be seen is, that usually at the end of the OCP measurement the potentials tend towards more a positive and stable value. This behavior is consistent with spontaneous passivation during OCP exposure in NaCl solution [6]. Whereas a gradual change towards more positive potentials indicates the formation of protective passive films on the surfaces, a stable potential suggests the stabilization and thickening of the passive film and the more positive the value the more stable the passive layer [15,74,75]. Furthermore, to theoretically assess the possible passivation for the studied materials the Pourbaix diagram of Ti, Nb and Ta in water were considered [76]. It shows that the various OCP for the studied materials are within the stable region of TiO₂, Nb₂O₅ and Ta₂O₅, hence the spontaneous formation of a passive layer can be expected from a thermodynamically point of view. However, the actual value and course of the curves differs depending on the material and surface condition. Both cp-Ti and Ti-6Al-4V reach a stable potential quicker and with a more positive value than Ti-42Nb and Ti-20Nb-6Ta when investigated with the as-built surfaces, indicating a better passivation behavior during the OCP measurements. With turned surfaces cp-Ti reaches a stable potential later than the β -type alloys and except for cp-Ti the materials show a similar course of their curves, but again both cp-Ti and Ti-6Al-4V have a more positive value, implying a more stable passive layer. However, with polished surfaces the OCP suggests a better passivation behavior for Ti-42Nb and Ti-20Nb-6Ta than Ti-6Al-4V.

The polarization curves of all four different Ti-based materials with and without machined surfaces are illustrated in Figs. 7–9 and several distinct features can be noticed. Between 1.721 and 2.140 V, the polarization curves exhibit a peak in current density for every material and surface condition. On the one hand, the cause of this anodic peak can be attributable to O₂ evolution [77], on the other hand a phase transformation in the passive oxide film from TiO₂ into TiO₃ [76] could be responsible. In Figs. 8 and 9 a low, but steady increase of the current density from a potential around 3 V is noticeable for cp-Ti and Ti-6Al-4V. Besides the possible occurrence of

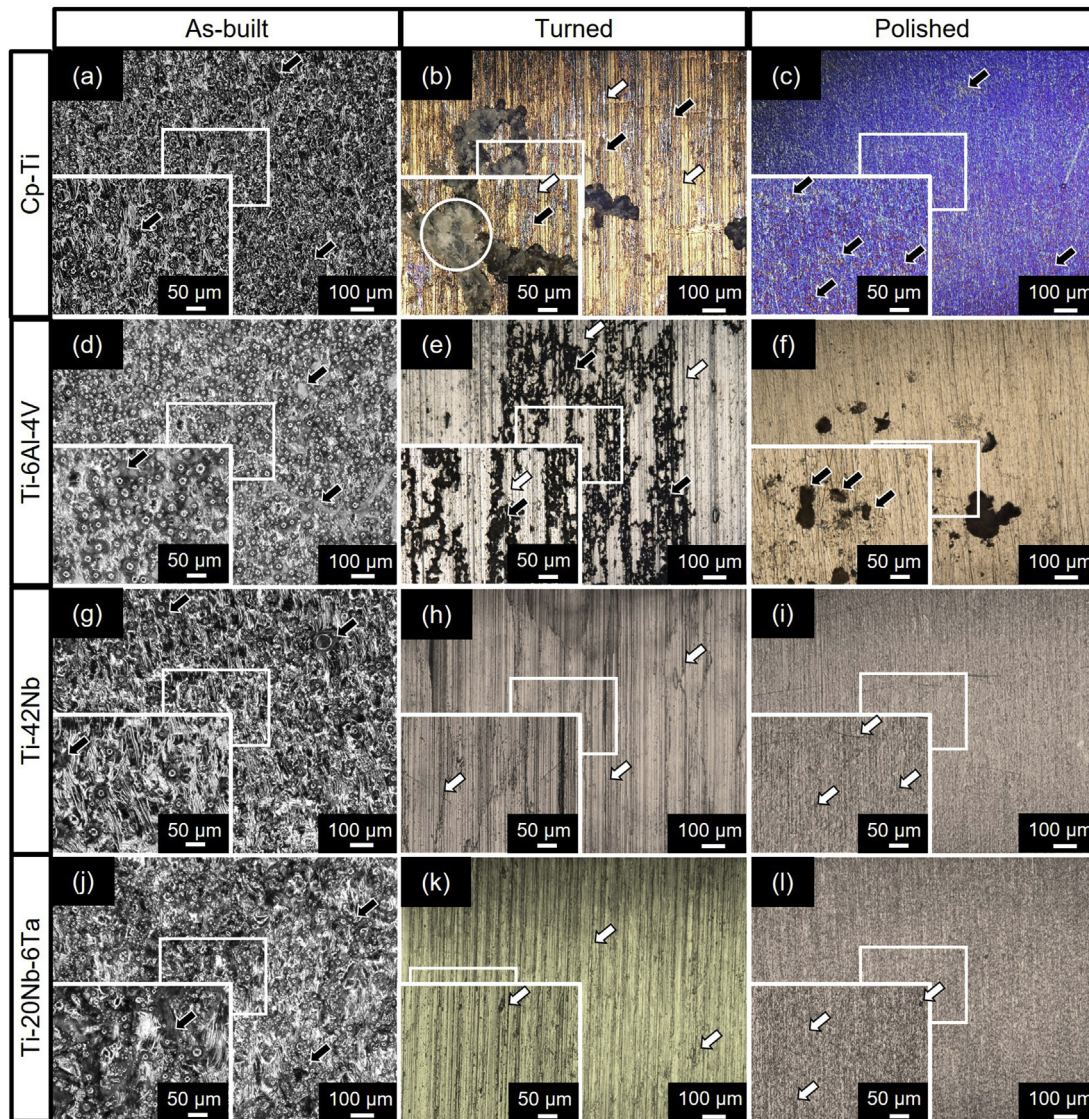


Fig. 10 – OM images of SLM-processed cp-Ti, Ti–6Al–4V, Ti–42Nb and Ti–20Nb–6Ta specimens with unmachined (as-built, left) and machined surfaces (turned middle, polished right) after polarization experiments.

crevice corrosion, for what no actual characteristics could be found on the surface of the specimens, this phenomenon could be caused by distinct metastable pitting. Burstein et al.

[78–80] showed in their work that at potentials well below the actual pitting potential the nucleation of corrosion pits can already occur on passive titanium, resulting in metastable pit

Table 6 – Surface condition and amount of released alloying elements during the corrosion experiments for the different materials.

Material	Al ($\mu\text{g/l}$)	V ($\mu\text{g/l}$)	Nb ($\mu\text{g/l}$)	Ta ($\mu\text{g/l}$)
Ti–6Al–4V				
As-built	64.442 ± 0.516	25.583 ± 0.128	–	–
Turned	3.955 ± 0.162	2.832 ± 0.031	–	–
Polished	13.708 ± 0.425	16.930 ± 0.796	–	–
Ti–42Nb				
As-built	–	–	0.413 ± 0.052	–
Turned	–	–	0.001 ± 0.001	–
Polished	–	–	0.001 ± 0.001	–
Ti–20Nb–6Ta				
As-built	–	–	0.003 ± 0.001	0.001 ± 0.001
Turned	–	–	0.001 ± 0.001	0.001 ± 0.001
Polished	–	–	0.001 ± 0.001	0.001 ± 0.001

Table 7 – Molybdenum Equivalency (MoE) for the different Ti-based materials (alloying elements in wt.%).

Material	MoE	Al	V	Nb	Ta	Fe
Cp-Ti	0.87	0.00	0.00	0.00	0.00	0.30
Ti–6Al–4V	–2.60	6.00	4.00	0.00	0.00	0.25
Ti–42Nb	11.93	0.00	0.00	42.00	0.00	0.06
Ti–20Nb–6Ta	7.04	0.00	0.00	20.00	6.00	0.04

propagation. This correlates well with the observations made by OM, as the surfaces of cp-Ti and Ti–6Al–4V are covered with lots of corrosion pits (Fig. 10b, c, e and f). Xia et al. [81] have reported similar observations. In Figs. 7–9 a small, but distinct peak at around -0.60 to -0.01 V can be detected for cp-Ti and Ti–6Al–4V. This is probably related to changes within the formed TiO_2 oxide layer [76]. This peak cannot be detected for Ti–42Nb and Ti–20Nb–6Ta as the two materials are alloyed with one or two other strong passive layer forming elements, Nb and Ta respectively, which oxide layer Nb_2O_5 and Ta_2O_5 show no changes at this potential range [76]. What is more, comparing the polarization curves of all four different Ti-based materials the missing transpassive region for the β -type Ti-alloys is very prominent. Even to a high potential of 10 V both alloys show no sign of a breakdown of the passive layer and pitting corrosion. Accordingly, no corrosion attack or anodic metallic dissolution marks could be observed on their surface, whereas for cp-Ti and Ti–6Al–4V distinct and prominent corrosion pits were clearly visible (Fig. 10a-l). Furthermore, when the influence of the surface roughness is reduced to a minimum (Fig. 9), E_{corr} is more noble as well as E_{crit} and E_{peak} are lower for Ti–42Nb and Ti–20Nb–Ta in comparison to cp-Ti and Ti–6Al–4V. A possible explanation is a better passivation behavior with quicker formation of more stable and dense passive layers for the β -type alloys at medium and high potentials due to the presence of Nb and Ta, as alloying elements can have a crucial influence on the passivation process. In general, titanium displays a good corrosion resistance due to its high affinity towards oxygen, that leads to the formation of a protective and self-repairing passive layer composing of TiO_2 [1,8]. If titanium is alloyed, the alloying elements also tend to form oxides that are integrated into the passive layer and lead to structural changes, which again can cause various types of point effects which influence the passivation properties and corrosion resistance of the alloy [10,11]. According to the Point Defect Model, the passive layer is denser, and therefore more stable, the less point defects are present [82]. A given example is Ti–6Al–4V, as V forms V_2O_5 and is embedded within the TiO_2 passive layer [14], but as V leads to defects in the layer and provides conduction channels, the general passivity of Ti–6Al–4V is corrupted in comparison to pure titanium [83]. In contrast, several studies have shown that other β stabilizing elements can significantly improve the corrosion resistance [6,11,83]. For example, Nb and Ta form Nb_2O_5 and Ta_2O_5 oxides that lead to less defects in the passive layer and an enhancement of its structural integrity as they decrease the concentration of anion vacancies in the layer [14,84]. In that case, they prevent the electron exchange more effectively [85,86], reduce the ingress of harmful chloride ions [87] and are more stable and less soluble compared to V_2O_5 [6,15]. As a result, the passive layers

of Ti–42Nb (Nb_2O_5) and Ti–20Nb–6Ta (Ta_2O_5) are presumably much denser, more stable and protective than the passive layers of cp-Ti and Ti–6Al–4V, thus preventing the occurrence of pitting corrosion until a potential of 10 V during electrochemical experiments. For one, this correlates well with the observed E_{corr} for the polished surfaces that are more noble for Ti–42Nb and Ti–20Nb–6Ta compared to cp-Ti and Ti–6Al–4V, since a higher value of E_{corr} indicates a more stable passive film [6,11]. Comparable results for similar and other β -type titanium alloys were found by Wang et al. [43], Zhukova et al. [88], Hussein et al. [89] and Dalmau et al. [90].

However, the corrosion resistance of the new β -type alloys is not completely superior. At first, although both Ti–42Nb and Ti–20Nb–6Ta show a lower i_{corr} than Ti–6Al–4V after surface machining, cp-Ti still has even lower corrosion current densities (Table 4) and higher polarization resistances (Table 5). Since a small value of i_{corr} and a high polarization resistance usually equal easy passivation [6,11,91,92], this means the passivation occurs more easily on Ti–42Nb and Ti–20Nb–6Ta than Ti–6Al–4V, but even more easily on cp-Ti. Moreover, within a certain potential range both materials display a more electrochemical active behavior, e. g. visible as higher current densities i_{pass} and i_{peak} (Table 4). The last phenomenon is probably attributed to deleterious microgalvanic cells, which can form due to electrical potential differences in the microstructure [74,93,94]. Since both new β -type alloys contain a large amount of alloying elements with very different standard electrode potentials compared to Ti [95,96], whereas cp-Ti and Ti–6Al–4V contain much fewer to none alloying elements, the probability of forming microgalvanic cells is much higher for Ti–42Nb and Ti–20Nb–Ta, which leads to accelerated corrosion processes and the observed higher current densities. However, if the passivation layer is formed the influence of these galvanic cells is considerably diminished, as no drastic increase of the current density or no transpassive region is observable (Figs. 7–9). That, again, is an indicator for the formation of very dense and stable oxide layers, as described before. A similar effect was observed by Atapour et al. [6] for a Ti–Mo–Zr–Fe β -type alloy, where the β stabilizing elements enhanced the stability of the passive layer, but showed no to almost detrimental effects on the corrosion resistance when no passive layer had formed.

Comparing only the two novel β -type alloys, both seem to display a similar corrosion resistance, but some differences are noticeable. With the turned surface Ti–20Nb–6Ta performs slightly better as the electrical potentials (E_{crit} , E_{peak}) and current densities (i_{pass} , $i_{\text{pass}2}$) are lower in comparison to Ti–42Nb, but with the polished surface Ti–42Nb shows better values than Ti–20Nb–6Ta. Furthermore, E_{corr} of Ti–42Nb is more noble and i_{corr} is lower in comparison to Ti–20Nb–6Ta for all surface condition that could implicate an easier passivation as well as a more stable passive layer for Ti–42Nb, as described before. A further difference is visible in regions with high electric potentials (6–10 V), where the current density of Ti–20Nb–6Ta starts to increase slowly at a steady rate. One reason for the better corrosion resistance of the Ti–42Nb alloy in comparison to the Ti–20Nb–6Ta alloy could be the microstructural composition. The β -phase Ti–42Nb performed better than the α'' -phase Ti–20Nb–6Ta, indicating a higher corrosion susceptibility for the martensitic

orthorhombic phase, which is in good understanding with other studies. For example, Oliveira et al. [97] investigated several Ti–Mo alloys, whereas an increasing amount of Mo led to a decreasing amount of α'' and an improvement of the corrosion resistance. Moraes et al. [98] and Guo et al. [99] added Sn in different concentrations to a Ti–30Nb and Ti–35Ta alloy, whereas certain amounts of Sn could both decrease the amount of α'' and simultaneously enhance the corrosion resistance. The improvement of corrosion resistance with the suppression of α'' by adding further alloying elements was also observed for Ti–22Nb–Hf [100], Ti–8Mo–Nb–Zr [101], Ti–Nb–O [102], Ti–30Nb–Fe [103] and Ti–30Nb–Zr [104,105]. Xia et al. [81] achieved an enhanced corrosion resistance of Ti–6Al–4V by adding Zr, however, above a certain amount of Zr α'' was formed and the corrosion resistance was impaired. Hariharan et al. [45] and Cremasco et al. [9] have shown, that different heat treatment processes of Ti–13Nb–13Zr and Ti–35Nb changed the microstructural composition and specimens with less amount of α'' exhibited a better corrosion resistance. Furthermore, the results indicate a more stable passive layer for Ti–42Nb, probably due to the higher amount of the β stabilizing elements or due to a possible detrimental effect of Ta on the structural integrity of the oxide layer. Apart from that, the formation of micro-galvanic cells could again play a substantial role. Ti–20Nb–6Ta consists of three different kinds of element with very different melting points. Element partitioning and constitutional undercooling could occur during the SLM process, which leads to an unfavorable elemental distribution and formation of nano-sized phases or clusters enriched in one element [49,50]. This circumstances and the different standard electrode potentials of the elements could favor the formation of galvanic cells and initiate pronounced corrosion processes for Ti–20Nb–6Ta in comparison to Ti–42Nb.

Finally, the influence of the surface condition and roughness can be clearly seen if Figs. 7–9 are compared. The SLM process leads to a high surface roughness, as residual powder particles are either partially melted or sintered onto the surface during the manufacturing process due to the laser beam focus diameter and heat affected zone [31]. For the SLM specimens with as-built surface morphology, all materials display a very fluctuating and rapidly increasing current density with several spikes until they reach a passive region at potentials of ca. 1.907–2.140 V. This behavior is not observable for the machined surfaces, which even show a passive region around 0.144–0.681 V. Furthermore, the passivation current density $i_{\text{pass}2}$ is the highest for the as-built surfaces for all four materials and decreases drastically, when the surface is machined. The more electrochemical active behavior of these surfaces can have different reasons. On the one hand, higher roughness induced by residual powder particles means a higher surface area, which can interact effectively with the surrounding electrolyte and participate in the electrochemical processes. As a result, many weak points that are susceptible to corrosion attacks and more potential metastable pitting starting points exist, consequently leading to the formation of more metastable corrosion pits and pronounced anodic metallic dissolution visible as spikes of the current density in the polarization curves (Fig. 7). Similar observations were made with SLM-

processed 316 L [106,107]. On the other hand, the high roughness of the as-built surfaces may form porous-like (foamy) structures, that lead to the formation of autocatalytic cells due to the accumulation of corrosion products within structures, that again favors localized metastable pitting [72]. The observed relation between surface morphology and corrosion resistance correlates well with other studies [66,108–111]. The consequence is visible for the released alloying elements that were analyzed after the corrosion experiments (Table 6). Ti–6Al–4V with the as-built surface morphology released roughly 5 to 16 times more Al and 1.5 to 8 times more V the specimen with the machined surface.

Within the frame of this work the corrosion resistance of four different titanium-based materials was investigated by potentiodynamic polarization and combined with mass-spectrometric analysis of released alloying elements as well as a microstructural characterization. However, there are certain limits to this study which need to be considered. Based on the polarization experiments the β -type alloys Ti–42Nb and Ti–20Nb–6Ta not only show a superior corrosion resistance, but also indicate an enhanced passivation behavior. However, to allow an in-depth evaluation of the passivation behavior a more detailed investigations of the formation, stability and constitution of the oxide layers with methods like X-ray photoelectron spectroscopy (XPS) or electrical impedance spectroscopy (EIS) is necessary and should be considered. Furthermore, the microstructural composition and elemental distribution play important roles with regard to the corrosion resistance as well as passivation behavior, for example considering the formation of micro-galvanic cells. Since SLM led to very fine structures and distributions, besides the performed investigations in this work a more detailed study is necessary. For example, the characterization with TEM or kelvin probe force microscopy (KPFM) would provide further insides.

5. Conclusions

The microstructure evolution, corrosion resistance and the amount of released alloying elements during corrosion experiments of two novel β -type titanium alloys, Ti–42Nb and Ti–20Nb–6Ta, were investigated and compared with commercially pure titanium grade 2 (cp-Ti) and the Ti–6Al–4V ELI alloy after SLM-processing. Furthermore, the influence of the SLM as-built surface as well as two machining processes on the corrosion resistance were investigated and compared. Within the limits of this study, the main conclusions can be drawn as follows:

- (1) Cp-Ti and Ti–6Al–4V crystallize completely in the martensitic hcp α' -phase during SLM. In case of Ti–42Nb, the amount of the β stabilizing element Nb was high enough to completely retain the bcc β phase until room temperature. In case of Ti–20Nb–6Ta, it did not contain enough β stabilizing elements and the orthorhombic martensitic α'' -phase was formed.
- (2) During the polarization experiments cp-Ti and Ti–6Al–4V underwent corrosion and showed a clear

transpassive region. In contrast, the β -type alloys showed no pitting corrosion or breakdown of the passive layer. This is probably attributed to the presence of tantalum oxides and/or niobium oxides and the improved passivation layer.

- (3) For Ti–6Al–4V high amounts of released Al and V were detected in the electrolytes after potentiodynamic polarization. In contrast, the β -type alloys Ti–42Nb and Ti–20Nb–6Ta released almost no alloying elements.
- (4) The corrosion resistance of Ti–42Nb and Ti–20Nb–6Ta is very similar with only slight distinctions. The passive layer of Ti–42Nb seems to be more stable under very high electrical potentials.
- (5) Surface machining of AM Ti alloys generally leads to lower surface roughness and a better corrosion resistance for all investigated materials, which is an important factor for achieving a good corrosion resistance.

Declaration of Competing Interest

The authors declare that they have no known competing financial interests or personal relationships that could have appeared to influence the work reported in this paper.

Acknowledgment

The authors would like to acknowledge the financial support from the German Federal Ministry for Education and Research BMBF for this research (Grant No. 13FH5I03IA). TANIOWIS GmbH is gratefully acknowledged for providing Ti–42Nb and Ti–20Nb–6Ta powder material. Eventually, the authors acknowledge support by the Open Access Publication Fund of the University of Freiburg.

REFERENCES

- [1] Leyens C, Peters M. *Titanium and titanium alloys: fundamentals and applications*. Weinheim, Chichester: Wiley VCH; 2010.
- [2] Boyer R, Welsch G, Collings EW. *Materials properties handbook: titanium alloys*. 4th ed. Materials Park, Ohio: ASM International; 2007.
- [3] Donachie MJ. *Titanium: a technical guide*. 2nd ed. Materials Park, OH: ASM International; 2000.
- [4] Lin C-W, Ju C-P, Chern Lin J-H. *Biomaterials* 2005;26:2899–907.
- [5] Mohsin Talib Mohammed, Zahid A. Khan, Arshad N. Siddiquee (2014).
- [6] Atapour M, Pilchak AL, Frankel GS, Williams JC. *Mater Sci Eng C* 2011;31:885–91.
- [7] Niinomi M. *Biomaterials* 2003;24:2673–83.
- [8] Bundy KJ. *Crit Rev Biomed Eng* 1994;22:139–251.
- [9] Cremasco A, Osório WR, Freire CM, Garcia A, Caram R. *Electrochim Acta* 2008;53:4867–74.
- [10] Geetha M, Kamachi Mudali U, Gogia A, Asokamani R, Raj B. *Corros Sci* 2004;46:877–92.
- [11] Bai Y, Li SJ, Prima F, Hao YL, Yang R. *Appl Surf Sci* 2012;258:4035–40.
- [12] Massalski TB, editor. *Binary alloy phase diagrams*. 2nd ed. Metals Park, Ohio: American Society for Metals; 1987.
- [13] Asri RIM, Harun WSW, Samykan M, Lah NAC, Ghani SAC, Tarlochan F, et al. *Mater Sci Eng C Mater Biol Appl* 2017;77:1261–74.
- [14] Metikoš-Huković M, Kwok A, Piljac J. *Biomaterials* 2003;24:3765–75.
- [15] Yılmaz E, Gökçe A, Findik F, Gulsoy H. *J Alloys Compd* 2018;746:301–13.
- [16] Matsuno H. *Biomaterials* 2001;22:1253–62.
- [17] Eisenbarth E, Velten D, Müller M, Thull R, Breme J. *Biomaterials* 2004;25:5705–13.
- [18] Mardare AI, Savan A, Ludwig A, Wieck AD, Hassel AW. *Corros Sci* 2009;51:1519–27.
- [19] Brodie EG, Medvedev AE, Frith JE, Dargusch MS, Fraser HL, Molotnikov A. *J Alloys Compd* 2020;820:153082.
- [20] Hon Y-H, Wang J-Y, Pan Y-N. *Mater Trans* 2003;44:2384–90.
- [21] Ozaki T, Matsumoto H, Watanabe S, Hanada S. *Mater Trans* 2004;45:2776–9.
- [22] Schulze C, Weinmann M, Schweigel C, Kefßler O, Bader R. *Materials* 2018;11.
- [23] Markhoff J, Weinmann M, Schulze C, Bader R. *Mater Sci Eng C Mater Biol Appl* 2017;73:756–66.
- [24] Kim HY, Fu J, Tobe H, Kim JI, Miyazaki S. *Shape Mem Superelasticity* 2015;1:107–16.
- [25] Kim HY, Hashimoto S, Kim JI, Inamura T, Hosoda H, Miyazaki S. *Mater Sci Eng, A* 2006;417:120–8.
- [26] Suenaga M, Ralls KM. *J Appl Phys* 1969;40:4457–63.
- [27] Inaekyan K, Brailovski V, Prokoshkin S, Pushin v, Dubinskiy S, Sheremetyev v. *Mater Char* 2015;103:65–74.
- [28] Pustov YA, Zhukova YS, Filonov MR. *Prot Met Phys Chem Surf* 2014;50:524–9.
- [29] Lyons B. *Bridge* 2014;44.
- [30] Böckin D, Tillman A-M. *J Clean Prod* 2019;226:977–87.
- [31] Kruth J-P, Dadbakhsh S, Vrancken B, Kempen K, Vleugels J, van Humbeeck J. In: Srivatsan TS, Sudarshan TS, editors. *Additive manufacturing: innovations, advances, and applications*. Boca Raton, Fla: CRC Press; 2016.
- [32] Herzog D, Seyda V, Wycisk E, Emmelmann C. *Acta Mater* 2016;117:371–92.
- [33] Colombo-Pulgarín JC, Biffi CA, Vedani M, Celentano D, Sánchez-Egea A, Boccardo AD, et al. *J Mater Eng Perform* 2021;30:6365–88.
- [34] Zhou YL, Niinomi M, Akahori T. *Mater Sci Eng, A* 2004;371:283–90.
- [35] Chen G, Yin J, Zhao S, Tang H, Qü X. *Int J Refract Metals Hard Mater* 2019;81:71–7.
- [36] Harun W, Kamariah M, Muhamad N, Ghani S, Ahmad F, Mohamed Z. *Powder Technol* 2018;327:128–51.
- [37] Liu S, Shin YC. *Mater Des* 2019;164:107552.
- [38] Zhang L-C, Attar H. *Adv Eng Mater* 2016;18:463–75.
- [39] Thijs L, Verhaeghe F, Craeghs T, van Humbeeck J, Kruth J-P. *Acta Mater* 2010;58:3303–12.
- [40] Xu Y, Lu Y, Sundberg KL, Liang J, Sisson RD. *J Mater Eng Perform* 2017;26:2572–82.
- [41] Cui Y-W, Chen L-Y, Qin P, Li R, Zang Q, Peng J, et al. *Corros Sci* 2022;203:110333.
- [42] Wysocki B, Maj P, Krawczyńska A, Roźniatowski K, Zdunek J, Kurzydłowski KJ, et al. *J Mater Process Technol* 2017;241:13–23.
- [43] Wang JC, Liu YJ, Qin P, Liang SX, Sercombe TB, Zhang LC. *Mater Sci Eng, A* 2019;760:214–24.
- [44] Vrancken B, Thijs L, Kruth J-P, van Humbeeck J. *Acta Mater* 2014;68:150–8.
- [45] Hariharan A, Goldberg P, Gustmann T, Maawad E, Pilz S, Schell F, et al. *Mater Des* 2022;217:110618.

- [46] Zhou L, Chen J, Huang W, Ren Y, Niu Y, Yuan T. *Vacuum* 2021;183:109798.
- [47] Luo X, Yang C, Li RY, Wang H, Lu HZ, Song T, et al. *Mater Sci Eng C Mater Biol Appl* 2021:112625.
- [48] Stern M, Geary AL. *J Electrochem Soc* 1957;104:56.
- [49] Stefanescu D, Ruxanda R. *Fundamentals of solidification*. 2004.
- [50] Kruth J-P, Levy G, Klocke F, Childs T. *CIRP Ann - Manuf Technol* 2007;56:730–59.
- [51] Gu D, Hagedorn Y-C, Meiners W, Meng G, Batista RJS, Wissenbach K, et al. *Acta Mater* 2012;60:3849–60.
- [52] Katzarov I, Malinov S, Sha W. *Metall Mater Trans* 2002;1027–40.
- [53] Zhou L, Yuan T, Tang J, He J, Li R. *Opt Laser Technol* 2019;119:105625.
- [54] Kumar P, Prakash O, Ramamurty U. *Acta Mater* 2018;154:246–60.
- [55] Kolli R, Devaraj A. *Metals* 2018;8:506.
- [56] Moffat DL, Kattner UR. *Metall Mater Trans* 1988;19:2389–97.
- [57] Lee CM, Ju CP, Chern Lin JH. *J Oral Rehabil* 2002;29:314–22.
- [58] Luo X, Li DD, Yang C, Gebert A, Lu HZ, Song T, et al. *Addit Manuf* 2022;51:102640.
- [59] Schwab H, Prashanth K, Löber L, Kühn U, Eckert J. *Metals* 2015;5:686–94.
- [60] Wang Q, Han C, Choma T, Wei Q, Yan C, Song B, et al. *Mater Des* 2017;126:268–77.
- [61] Tang X, Ahmed T, Rack HJ. *J Mater Sci* 2000;35:1805–11.
- [62] Aiyangar AK, Neuberger BW, Oberson PG, Ankem S. *Metall Mater Trans* 2005;36:637–44.
- [63] Ramesh A, Ankem S. *Metall Mater Trans* 2002;33:1137–44.
- [64] Sivakumar B, Pathak LC, Singh R. *Appl Surf Sci* 2017;401:385–98.
- [65] Pedre D, Li M, Poleske T, Mozaffari-Jovein H. The Canadian institute of mining, metallurgy and petroleum. In: *Proceedings of the 59th conference of metallurgists, COM 2020: the Canadian institute of mining, metallurgy and petroleum, Canada; 2020*. p. 1391–405.
- [66] Li M, Pedre D, Poleske T, Mozaffari-Jovein H. *Adv Metallurg Mater Eng* 2020;3.
- [67] Zhang B, Li Y, Bai Q. *Chin J Mech Eng* 2017;30:515–27.
- [68] Cao F, Shi Z, Song G-L, Liu M, Dargusch MS, Atrens A. *Corros Sci* 2015;94:255–69.
- [69] Seah K, Thampuran R, Teoh SH. *Corros Sci* 1998;40:547–56.
- [70] Yang D, Kan X, Gao P, Zhao Y, Yin Y, Zhao Z, et al. *Appl Phys A* 2022;128.
- [71] Sander G, Thomas S, Cruz V, Jurg M, Birbilis N, Gao X, et al. *J Electrochem Soc* 2017;164:C250–7.
- [72] Song G, Atrens A, Dargusch M. *Corros Sci* 1998;41:249–73.
- [73] Song GL, St John DH, Abbott T. *Int J Cast Metals Res* 2005;18:174–80.
- [74] Lu J, Ge P, Li Q, Zhang W, Huo W, Hu J, et al. *J Alloys Compd* 2017;727:1126–35.
- [75] Qin P, Liu Y, Sercombe TB, Li Y, Zhang C, Cao C, et al. *ACS Biomater Sci Eng* 2018;4:2633–42.
- [76] Pourbaix M. *Biomaterials* 1984;5:122–34.
- [77] Mareci D, Ungureanu G, Aelenei DM, Rosca JCM. *Mater Corros* 2007;58:848–56.
- [78] Burstein GT, Liu C, Souto RM. *Biomaterials* 2005;26:245–56.
- [79] Burstein GT, Liu C. *Corros Sci* 2007;49:4296–306.
- [80] Burstein GT, Liu C. *Corros Sci* 2008;50:2–7.
- [81] Xia C, Zhang Z, Feng Z, Pan B, Zhang X, Ma M, et al. *Corros Sci* 2016;112:687–95.
- [82] Macdonald DD. *J Electrochem Soc* 1992;139:3434–49.
- [83] Lavos-Valereto IC, Wolyneec S, Ramires I, Guastaldi AC, Costa I. *J Mater Sci Mater Med* 2004;15:55–9.
- [84] Li J, Li SJ, Hao YL, Huang HH, Bai Y, Hao YQ, et al. *Acta Biomater* 2014;10:2866–75.
- [85] Wang YB, Zheng YF. *Mater Lett* 2009;63:1293–5.
- [86] Zhou YL, Niinomi M, Akahori T, Fukui H, Toda H. *Mater Sci Eng, A* 2005;398:28–36.
- [87] Oliveira NT, Ferreira EA, Duarte LT, Biaggio SR, Rocha-Filho RC, Bocchi N. *Electrochim Acta* 2006;51:2068–75.
- [88] Zhukova YS, Pustov YA, Konopatsky AS, Filonov MR. *J Alloys Compd* 2014;586:S535–8.
- [89] Hussein AH, Gepreel MA-H, Gouda MK, Hefnawy AM, Kandil SH. *Mater Sci Eng C, Mater Biol Appl* 2016;61:574–8.
- [90] Dalmau A, Guinón Pina V, Devesa F, Amigó v, Igual Muñoz A. *Mater Sci Eng C, Mater Biol Appl* 2015;48:55–62.
- [91] Toshev Y, Mandova V, Boshkov N, Stoychev D, Petrov P, Tsvetkova N, et al. In: *4M 2006 – Second international conference on multi-material micro manufacture*. Elsevier; 2006. p. 323–6.
- [92] Fu T, Zhan Z, Zhang L, Yang Y, Liu Z, Liu J, et al. *Surf Coating Technol* 2015;280:129–35.
- [93] Maya-Johnson S, López D. *Mater Des* 2014;58:175–81.
- [94] Yang Y, Xia C, Feng Z, Jiang X, Pan B, Zhang X, et al. *Corros Sci* 2015;101:56–65.
- [95] Bard AJ, Parsons R, Jordan J, editors. *Standard potentials in aqueous solution*. New York: Dekker; 1985.
- [96] Greenwood NN, Earnshaw S. *Chemistry of the elements*. Elsevier; 1997.
- [97] Oliveira NT, Aleixo G, Caram R, Guastaldi AC. *Mater Sci Eng, A* 2007;452–453:727–31.
- [98] Moraes PE, Contieri RJ, Lopes ES, Robin A, Caram R. *Mater Char* 2014;96:273–81.
- [99] Guo B, Tong YX, Chen F, Zheng YF, Li L, Chung CY. *Mater Corros* 2012;63:259–63.
- [100] Wang BL, Zheng YF, Zhao LC. *Mater Corros* 2009;60:330–5.
- [101] Nnamchi PS, Obayi CS, Todd I, Rainforth MW. *J Mech Behav Biomed Mater* 2016;60:68–77.
- [102] Wang J, Xiao W, Ren L, Fu Y, Ma C. *Mater Char* 2021;176:111122.
- [103] Lopes ÉSN, Salvador CAF, Andrade DR, Cremasco A, Campo KN, Caram R. *Metall Mater Trans* 2016;47:3213–26.
- [104] Martins DQ, Souza M, Souza SA, Andrade DC, Freire C, Caram R. *J Alloys Compd* 2009;478:111–6.
- [105] Martins DQ, Osório WR, Souza ME, Caram R, Garcia A. *Electrochim Acta* 2008;53:2809–17.
- [106] M. Conte, C. Gelsomini, R. Franci, R. Giovanardi 22 (2019) N/A–N/A. *J Corrosion Sci Eng*.
- [107] Wang H, Shu X, Zhao J. *Materials* 2022;2022.
- [108] He X, Noël JJ, Shoemith DW. *Corrosion* 2004;60:378–86.
- [109] Codaro E, Nakazato R, Horovistiz A, Ribeiro L, Ribeiro R, Hein L. *Mater Sci Eng, A* 2003;341:202–10.
- [110] Atapour M, Pilchak A, Frankel GS, Williams JC, Fathi MH, Shamanian M. *Corrosion* 2010;66.
- [111] Li W, Li DY. *Acta Mater* 2006;54:445–52.